Kent Academic Repository
Full text document (pdf)

Link to record in KAR

https://kar.kent.ac.uk/57821/

Document Version

Author's Accepted Manuscript

A search for ionized jets towards massive young stellar objects

S. J. D. Purser,[1]⋆ S. L. Lumsden,[1] M. G. Hoare,[1] J.S. Urquhart,[2,3] N. Cunningham,[1,4]
C.R. Purcell,[5] K.J. Brooks,[6] G. Garay,[7] A.E. Gúzman[7] and M.A. Voronkov[6]

[1]*School of Physics and Astronomy, University of Leeds, Leeds LS2 9JT, UK*
[2]*Max-Planck-Institute für Radioastronomie, Auf dem Hügel 69, D-53121 Bonn, Germany*
[3]*Centre for Astrophysics and Planetary Science, The University of Kent, Canterbury, Kent CT2 7NH, UK*
[4]*National Radio Astronomy Observatory, PO Box 2, Green Bank, WV 24944, USA*
[5]*Sydney Institute for Astronomy (SIfA), School of Physics, The University of Sydney, NSW 2006, Australia*
[6]*Australia Telescope National Facility, CSIRO Astronomy and Space Science, PO Box 76, Epping, NSW 1710, Australia*
[7]*Departamento de Astronomía, Universidad de Chile, Casilla 36-D, Santiago, Chile*

ABSTRACT

Radio continuum observations using the Australia telescope compact array (ATCA) at frequencies of 5.5, 9.0, 17.0 and 22.8 GHz have detected free-free emission associated with 45 out of a sample of 49 massive young stellar objects and HII regions. Of these, 26 sources exhibit the characteristics of ionized jets, 2 exhibited features common to both disc-winds and ionized jets, 1 exhibits those of a disc-wind, 14 exhibit those of ionized HII regions and 2 were unable to be categorised. Classification of these objects as ionized jets is based upon their elongated or lobe-like morphologies, radio fluxes and/or radio spectral indices across the observed frequencies, in conjunction with the cross-correlation with observations at other wavelengths. In 50% of the ionized jets, further associated emission is seen in the form of spectrally flat/non-thermal lobes likely representing working surfaces whereby jet material impinges upon the cavity walls or internal shocks within the jet. Ten of the thirteen jets display non-thermal spectra in the associated lobes (from synchrotron emission), with an average spectral index in these cases of $\alpha = -0.53$. This shows that magnetic fields are present in a large percentage of ionized jets, in agreement with models of ionized jet formation incorporating magnetic fields. Since the production of collimated radio jets is intimately associated with accretion processes, the results presented in this paper support the picture of clump-fed, disc-mediated accretion for the formation of massive stars with a jet phase lasting approximately $6.5 \times 10^4\,$yr. Assuming fixed ionization fractions of 0.2 and terminal jet velocities of 500 km s^{-1}, typical mass loss rates in the jet are found to be $2.7 \times 10^{-5}\,$M$_\odot$ yr^{-1} with associated momentum rates of the order $2 \times 10^{-2}\,$M$_\odot$km s^{-1} yr^{-1}.

Key words: stars: formation, stars: massive, stars: protostars, ISM: jets and outflows, radio continuum: ISM, surveys

1 INTRODUCTION

The formation of massive stars still presents a problem in astrophysics today. With their powerful outflows and radiative outputs, they play a significant role in local (cloud/clump scale) as well as galactic evolution, thus understanding massive young stellar objects (MYSOs) and their formation is of critical importance. Current theories on the exact mechanisms of formation include the incorporation of accretion through discs (McKee & Tan 2002), similar to the low-mass paradigms of Shu et al. (1987), as well as a competitive accretion scenario whereby the size of the reservoir of accreted material onto a MYSO's disc stems from the gravitational potential in which it resides (Bonnell et al. 2001a,b). Due

to sampling/observational constraints (a by-product of the comparative rarity and extreme distances of massive stars), only a few cases of accretion discs around massive stars have been observed, most notably the disc imaged through near-infrared interferometry by Kraus et al. (2010) around the massive young stellar object, IRAS 13481−6124 (G310.0135+00.3892 in this paper). With the advent of ALMA however, we expect this type of observation to become more common. One such example is that of the MYSO G345.4938+01.4677 (Guzmán et al. 2014) which showed evidence in SO$_2$ molecular lines of a rotating disc structure perpendicularly oriented to the previously established ionized jet (Guzmán et al. 2010).

For this work, we turn our attention towards the larger scale jets of ionized material moving away from, and perpendicular to, the disc. As well as carrying away excess angular momentum

⋆ E-mail: pysjp@leeds.ac.uk

(avoiding terminal 'spin-up' of the protostar), they also provide a source of momentum to drive/entrain large-scale molecular outflows, almost ubiquitously associated with sites of massive star formation (Beuther et al. 2002). With their detection, they provide indirect evidence for the accretion process itself, while measurement of jet velocities, momenta and mass loss rates (Eisloffel et al. 2000) can provide an insight into the exact accretion mechanisms in operation. In turn this may aid in differentiating between competitive/Bondi-Hoyle accretion (Bonnell et al. 2001a) and turbulent core accretion models (McKee & Tan 2002).

Ideas put forward to explain both the production and collimation of ionized jets from massive stars are based upon those of their low-mass counterparts. Mechanisms have been suggested, which can be categorised as either being driven purely in the disc, or by disc/stellar wind interactions.

A pure disc-wind model was produced by Blandford & Payne (1982), who suggested that a poloidal magnetic field originating from the accretion disc itself, would act as a launching mechanism for ionized material travelling inwards in the disc. This material would travel along the field lines and away from the disc, accurately adhering to the analogy of 'beads on a wire'. As the accretion disc rotates, these field lines become more twisted (due to magnetic coupling) further from the disc and eventually collimation is induced by 'hoop stresses' from the field upon the ionized material. Simulations by Seifried et al. (2012) showed that massive protostellar jets were likely driven by this mechanism, with varying hoop stresses (enhanced by weaker magnetic fields, and suppressed by sub-Keplerian disc motions in the presence of strong fields) in the disc affecting the degree of collimation. This result predicted that collimation should relate to the evolutionary stage of the MYSO (i.e. lower degrees of collimation for younger MYSOs).

On the other hand, Shu et al. (1994) proposed a model involving both stellar, and disc magnetic fields, referred to as the 'X-wind model'. This is so named because the launching radius for the jet in the disc is located at the X-shaped lines of equipotential (balancing points of gravitational and centrifugal forces) located near the truncated (by strong stellar magnetic fields), inner surface of the disc itself. With the inward flow of material in the accretion disc, magnetic coupling bows the field lines inwards. Consequently, this inflowing material follows these field lines up and away from the disc. Magneto-centrifugal processes accelerate the gas supersonically in a direction parallel to the poloidal field lines, resulting in an outflowing wind. Twisted magnetic fields further away from the disc's mid-plane focus the ionized material, resulting in a collimated, ionized jet. When applied to massive star formation, the X-wind model presents a problem however. Stellar magnetic fields are intrinsically related to the convective nature of their protostars. For low-mass protostars, these convective models adhere well to reality with the onset of deuterium burning (Stahler 1988). Simulations of the protostellar evolution of MYSOs, (e.g. Hosokawa & Omukai 2009) show them to evolve through radiative as well as convective stages, so this phase is much more limited in time.

The observation by Carrasco-González et al. (2012) of polarised emission from an ionized jet associated with the HH 80-81 object, revealed possible poloidal field lines, suggesting a magnetic mechanism for jet formation around MYSOs. However, this type of result is not common in the literature, and the formation of jets around massive protostars is still an open question.

Observationally, much information can be gleaned from measurement of the spectral index of a jet's free-free radio emission. A paper by Reynolds (1986) derived the following relationships between a jet's physical parameters:

$$\alpha = 2 + \frac{2.1}{q_\tau}\left(1 + \epsilon + q_T\right) \tag{1}$$

$$\alpha = \frac{4\beta - 6.2}{2\beta - 1} \tag{2}$$

Where α is the spectral index ($S_\nu \propto \nu^{-\alpha}$), ϵ represents the degree of collimation and q_T and q_τ are essentially the powers to which the temperature and optical depth in the jet vary with distance from the base of the jet. For equation 2, $n_e \propto r^{-\beta}$ where n_e is the number density of electrons, and r is the distance from the MYSO).

For a standard (i.e. not accelerating or recombining), biconical jet, a spectral index of ~ 0.6 is expected, however spectral indices of $-0.1 \rightarrow 1.6$ are found when considering a variety of jet scenarios. Although the derivation of the spectral index cannot be used to infer temperature or density profiles along the jet, we can deduce information about the jet's geometry (collimation) and processes likely ongoing within the flow (such as further acceleration or recombination for example), as summarised in Table 1 of Reynolds (1986). As well as the spectral index, we can measure the behaviour of the deconvolved major axis of the jet with frequency (which is dependent upon the relationship between electron density and radial distance from the powering source), i.e. $\theta_{maj} \propto \nu^\gamma$, where θ_{maj} is the deconvolved major axis and γ is the measured index. For a conical wind ($\alpha = 0.6$), we expect $\gamma = -0.7$ as can be seen from equations 2 and 3, demonstrating the connection between these two variables.

$$\gamma = -\frac{2.1}{2\beta - 1} \tag{3}$$

Specific examples of radio jets in the literature, associated with sites of high mass star formation, are those of HH 80-81 (G010.8411−02.5919) and Cepheus HW-2. These MYSOs harbour thermal jets found to have proper motions of $\sim 500\,\mathrm{km\,s^{-1}}$, and $\sim 480\,\mathrm{km\,s^{-1}}$ (Martí et al. 1998; Curiel et al. 2006, respectively), which are much greater than the velocities typically seen in low-mass cases of $\sim 200\mathrm{km\,s^{-1}}$ (Arce et al. 2007). Cepheus HW-2 consists of a simple elongated structure with a spectral index of $\alpha = 0.69 \pm 0.06$, indicative of a conical bipolar jet (Rodriguez et al. 1994). Conversely HH 80-81 consists of a more complex picture whereby a central, thermal source ($\alpha \sim 0.2$) and two non-thermal lobes ($\alpha \sim -0.3$) align on a NE-SW orientation (Marti et al. 1993). These two examples show the range of complexities which radio observations of ionized jets reveal.

Systematic searches for ionized jets are few and far between, and conducted with sporadic success. Gibb & Hoare (2007) performed radio observations from 5 to 43 GHz towards 5 MYSOs with spectral indices ranging from 0.2 to 0.8, all consistent with ionized jets/winds (Reynolds 1986). Although no jets were definitively identified, two sources (S106-IR and S140-IRS1), whose radio emission was perpendicular to their associated molecular outflows, were classified as equatorial disc winds. Another survey by Guzmán et al. (2012), detected two radio jets (G343.1261-00.0623 and G345.4938+01.4677 in this paper) from a sample of 33 (8 of which were observed) IR-luminous objects taken, in part, from the RMS survey (see §2.1). An issue with this survey's sampling methodology, was selection criteria based upon positive radio spectral indices and low radio to IR luminosities, the radio data for which was taken from Walsh et al. (1998) and Urquhart et al. (2007). This resulted in contamination of the sample by unresolved, optically-thick HII regions with low radio fluxes, which

were under-luminous compared to radio fluxes expected from the bolometric luminosities (for an optically thin HII region). The survey's 4σ detection limits were ~ 0.8 mJy, at 1.4 and 2.4 GHz and ~ 0.4 mJy, at 4.8 and 8.6 GHz. Since we expect radio-weak, thermal spectra from the ionized jets, at those frequencies emission from such objects may have remained undetected. Most recently Moscadelli et al. (2016) selected a sub-sample of MYSOs (ZAMS type B3-O7) from the Bar and Spiral Structure Legacy (BeSSeL) survey, which displayed water maser activity, and previous compact ($< 1''$), and weak (which they define as < 50 mJy) radio emission. Of the 40 objects in the sample, 11 were observed with the VLA at C, K and Ku-bands ($\theta_{res} \sim 0.2''$), 10 displayed spectral indices typical of thermal jets, 5 of which were confirmed to have collimated (opening angles, θ_0, of between 10 and $30°$) outflows via maser kinematics. Spectral indices ranged between $0.1 \leqslant \alpha \leqslant 1.1$, with inferred momentum rates of between 10^{-3}-$-1\,M_\odot \mathrm{kms}^{-1}\mathrm{yr}^{-1}$. Interestingly, lobes of elongated, non-thermal emission were observed towards two of the sample, suggestive of the presence of magnetic fields.

With these previous ionized jet surveys in mind, our own RMS survey-derived selection of targets, in conjunction with the targets of Guzmán et al. (2012), was used to create an unbiased sample of MYSOs which could harbour ionized jets.

In this paper, we introduce the methodology of our sample selection (§2), and explain the technicalities of its observation in §3.1. Section 4 contains a discussion of cleaned and imaged radio data (Figure C1 in the online version) and their relation to previous observations within the literature. This is done for a selection of specific examples representative of the sample as a whole. An overall, statistical approach is then employed in §5, from which implications to current jet and accretion models are discussed. These findings are summarised in §6.

2 A SAMPLE OF MYSOS

2.1 The RMS survey

The Red MSX Source survey (Lumsden et al. 2013) is a systematic search for MYSOs using previous surveys as well as mm, radio and infrared follow-up observations to aid in the classification of objects catalogued by the Midcourse Space eXperiment (MSX; Price et al. 2001). This extensive, ordered approach was necessary considering the relative sparsity of forming massive stars in the Galaxy.

In order to extract genuine MYSO candidates from the MSX database, contaminant objects such as planetary nebulae, old dusty stars and resolved ultra-compact HII regions had to be removed. Since most of the bolometric luminosity of a MYSO lies at infrared wavelengths (due to dust reprocessing), a comparison of fluxes at a variety of IR-wavelengths (based on known MYSOs) was employed. The exact sampling methodologies used can be found in Lumsden et al. (2002).

VLA (Urquhart et al. 2009) and ATCA (Urquhart et al. 2007) observations at 5 GHz ($\theta_{res} \sim 1''$) helped to remove compact UCHIIs, while mm observations by MOPRA ($^{13}CO(1-0)$) and JCMT ($^{13}CO(2-1)$) allowed the removal of close, low-mass YSOs by the determination of kinematic distances and therefore absolute luminosities (Urquhart et al. 2007). The relative strength of the CO lines helped eliminate dusty, evolved stars (stronger in young stars) while those evolved stars lying along the line of sight to H_2 molecular clouds were picked out on the basis of their distinct near-IR absorption spectra.

The resulting RMS database[1] catalogues ~ 900 embedded, young massive stars (Urquhart et al. 2014) of which both HII regions and MYSOs are included.

2.2 Sample selection

In total, we have a sample of 49 individual objects which are listed in Table 2. Of these, 34 were selected to form a distance-limited (d < 7kpc) sample of MYSOs. An even spread in the luminosities of the objects was required for unbiased sampling in terms of bolometric luminosity and consequently 6 of these objects fall in the range $700\,L_\odot \leqslant L_\star < 3000\,L_\odot$, 11 in the range $3000\,L_\odot \leqslant L_\star \leqslant 10000\,L_\odot$, 9 in the range $10000\,L_\odot \leqslant L_\star \leqslant 30000\,L_\odot$ and 8 with $L_\star > 30000\,L_\odot$. It is worth noting that derived bolometric luminosities have changed for some of the sample since the observations. The previous observations of Urquhart et al. (2007) have demonstrated them all to be radio weak with $S_\nu < 2$ mJy. These sources are at elevations conducive to more circular synthetic apertures, whereby $\delta < -34°$. Targets with declinations greater than the quoted cut-off have been included due to their scientific value, as well as filler objects for allocated times when the other sources were not fully risen above the horizon (i.e. elevation $< 20°$). A further 8 objects were added to complete the observations (at 17 and 22.8 GHz) which Guzmán et al. (2012) performed from 1.4 to 8.6 GHz with the ATCA. One of the Guzman sample (G317.4298-00.5612) was observed at 5 and 9 GHz to check for variability. Four of the objects were added on the basis of being associated to 4.5 µm excesses, or extended green objects (EGOs Cyganowski et al. 2008), a signature of shocks possibly caused by jet activity (Smith & Rosen 2005). The latter two samples were not distance-limited and also were used to fill in coverage in right ascension.

3 OBSERVATIONS AND DATA REDUCTION

3.1 Radio observations with the ATCA

All radio observations were made using the Australia Telescope Compact Array (ATCA; See chapter 1, §1 of Frater et al. 1992, for an overview) in the 6A and 6B configurations, over a period of 12 days, spread over 4 years. A total of 49 individual, compact objects were observed at 4 different frequency bands (centred on 5.5, 9.0, 17.0 and 22.8 GHz). These frequencies were observed using a bandwidth of 2048 MHz (XX, YY, XY, and YX polarizations) split evenly either side of the central frequencies (an overview of the CABB correlator's capabilities can be found in Wilson et al. 2011). This bandwidth was split into channels of width 1 MHz (minimising the averaging out effect of RFI over broad channels and giving the ability to easily recognise and flag it). From this point on the frequency bands observed shall be referred to as 5.5, 9, 17 and 22.8GHz bands.

The highest frequency band has been also chosen to incorporate the $H_2O(6 \rightarrow 5)$ transition at 22.235 GHz, in order to observe masing activity and allow more accurate, phase-only self-calibration from the relevant channels.

Throughout the radio bands, radio recombination lines should also be observable in the strongest sources, giving some degree of kinematic information for the ionized gas. Table 1 shows the radio recombination lines falling within the observed bands, and their effective, velocity resolutions for a channel width of 1 MHz.

---

[1] http://rms.leeds.ac.uk/cgi-bin/public/RMS_DATABASE.cgi

Band (GHz)	RRLs	$\Delta\mathrm{v}$ (km s^{-1})
5.5	H100α − H112α	54.5
9	H87α − H93α	33.3
17	H71α − H73α	17.6
22.8	H65α, H66α	13.1

Table 1. A table of the observable radio recombination lines for each observed band, and the associated resolution per 1 MHz channel (at the centre of each band).

The range of scales the instrument was sensitive to were 2.0-−16.5″, 1.2 − 10.1″, 0.6 − 5.4″ and 0.5 − 4.0″ over the 5.5, 9, 17 and 22.8 GHz frequency bands respectively. These correspond to a maximum baseline length of 6 km and a minimum of ∼ 300 m.

Individual scan times on flux and phase calibrators were 5 minutes and 90 seconds respectively and on target sources were between 5 and 20 minutes dependent on atmospheric conditions and observing frequencies. The average total integration time on each science target, τ_{int}, was ∼ 75 minutes. Observations at 5.5 and 9 GHz were all conducted during February 2013, with a typical RMS noise level calculated to be 17 and 20 μJy/beam respectively. The upper two frequency bands were observed during the months of February 2010, April 2011, September 2011 and January 2012, giving a range of conditions particularly affecting the 22.8 GHz band which is more sensitive to atmospheric water vapour content (greater during the southern hemisphere's summer months). Theoretical RMS noise levels therefore range between 40 − 41 and 73-−106 μJy/beam for the 17 and 22.8 GHz bands respectively, during the months of September (lower noise) and January. As a note, the typical values for the RMS noise were calculated assuming the removal of 200 channels (100 at each edge of the bandwidth), RFI interference, typical weather during the relevant months, $\delta \sim -50°$ and a robustness of 0.

3.2 Data reduction

For calibrating and cleaning the data, the Multichannel Image Reconstruction Image Analysis and Display (MIRIAD) software package (Sault et al. 1995) was used. For the measurement of various parameters, the Common Astronomy Software Applications (CASA) was implemented (McMullin et al. 2007).

Multi frequency synthesis was used to image the visibility datasets, and at 5.5, 9 and 17 GHz, the multi-frequency CLEAN algorithm (MFCLEAN in miriad) was used to account for the variation in intensity distribution with frequency, since the fractional bandwidth is >12.5% (Sault & Wieringa 1994). In Fourier transforming the data, the visibilities were weighted according to T_{sys} in order to down-weight data taken at times of increased atmospheric instability and thus improve the signal-to-noise ratio of the resultant images. This acted to improve the accuracy of recorded fluxes, at the cost of more elongated restoring beams.

Phase only self-calibration was performed on any strong point source (extended sources give erroneous solutions for the limited baseline numbers of the ATCA) in the field of view, and solutions were applied only if they converged over the course of multiple iterations (in terms of the rms deviations on the gain phases). Time intervals over which to produce calibration solutions took account of the calibrating source's flux and the frequency of the observations (since the atmosphere is more stable at lower frequencies). At

22.8 GHz, if masing activity was present for the 22.23508 GHz water line, the strongest channel was imaged and used as a model for phase-only self-calibration. Simultaneous amplitude and phase self calibration was not performed on any of the datasets since there are not enough constraints with 15 baselines to solve for both the real and imaginary parts of the gains.

3.3 Measurement of fluxes and spectral indices

For the clean images of our observed fields, both resolved and unresolved emission had to be measured. Thus, integrated radio flux measurements on sources in the field/pointing centre were performed in one of two ways, dependent on this morphology. For simple (i.e. Gaussian-like, both resolved and compact) morphologies, the CASA task, IMFIT, was used to measure the deconvolved dimensions, positions and fluxes. IMFIT works by the fitting of one/several Gaussian profile(s) to the image plane (from a roughly guessed model), whose properties estimate those of the source. Residual maps of the Gaussian model(s) subtracted from the real emission were consequently inspected to make sure that no components were unaccounted for (i.e. the residual map is 'noise-like'). For extended and non-Gaussian morphologies the fluxes were integrated over the 3σ flux area, positions were taken as the peak emission's location and deconvolved dimensions were measured using equation 4 below.

$$\theta_{\mathrm{G}} = \sqrt{\theta_{\mathrm{source}}^2 - \theta_{\mathrm{beam}}^2} \qquad (4)$$

where θ_{G} is the deconvolved size of the source, θ_{source} is the measured FWHM of the source and θ_{beam} is the FWHM of the restoring beam.

The image rms deviation was measured in portions of the field without emission, close to the source (so residual artefacts from the cleaning process, such as side lobes, were included in the noise estimation).

The measurement of spectral indices for each source was performed using least squares fitting algorithms. Errors on the fluxes included those provided by the noise/Gaussian fit parameters in addition to a generally accepted 10% error on the absolute flux calibration of the ATCA. In the case where only two frequencies are present, the spectral index is estimated from the difference between each flux, whose associated error is estimated by combining the fluxes' errors (plus the previously mentioned 10%) in quadrature. Similar techniques are used for the derivation of the power-law index associated to the variation of major axis length with frequency, γ.

As a note, thermal sources are defined as those possessing a spectral index of $\alpha \geqslant -0.1$ and are assumed to be dominated by thermal Bremsstrahlung, while non-thermal sources have $\alpha < -0.1$ and are assumed to be dominated by synchrotron emission. We define the optically thin and thick regimes for free-free emission as $-0.1 \leqslant \alpha \leqslant 1$ and $1 < \alpha \leqslant 2$ respectively.

3.4 Flux recovery with the 6km configuration

As a check, modelling was performed on a synthetic dataset in order to calculate how much flux is resolved out at each observing frequency. This is an expected effect of interferometry, since the shortest baseline (in units of wavelength) increases in size with increasing frequency and consequentially, the array's scale-sensitivity drops at larger spatial scales.

Table 2. Target sources observed by ATCA between 12/02/2010 and 28/02/2013, their bolometric luminosities and distances (Lumsden et al. 2013). Sample selection is indicated by the superscripted symbol on each source's name, whereby ⋆ indicates a filler object of scientific value, † indicates an object which is part of the Guzmán et al. (2012) sample and ‡ indicates an MYSO associated to an EGO (Cyganowski et al. 2008). Any source without a symbol is part of the distance limited sample. The footnote marks for the distances indicate how they were calculated: a) kinematic distance determined using the source velocity; b) spectrophotometric distance; c) maser parallax distance; d) distances taken from the literature. The footnote marking for the bolometric luminosities show the relevant calculation methods which were: a) spectral energy distribution (SED) fit to the available infrared fluxes (e.g., 2MASS, MSX) including HiGAL (Mottram et al., in prep.); b) SED fit to infrared and either MIPSGAL 70μm or IRAS Galaxy ATLAS 60μm fluxes (Mottram et al. (2010), Mottram et al. (2011)); c) MSX 21μm band flux using a scaling relationship determined from a comparison with sources where SED fits have been possible (Mottram et al. 2011). Also included are the epochs during which their data was recorded by the ATCA for the 5/9 GHz setup and 17/22.8 GHz setup. The epoch notation corresponds to the following dates: E1, 12/02/2010-13/02/2010; E2, 16/04/2011; E3, 10/09/2011-11/09/2011; E4, 05/01/2012-07/01/2012; E5, 25/02/2013-28/02/2013. Date ranges include all dates in between those provided. Hyphenated table cells denote the source not being observed at the relevant frequencies. The final column denotes each object's final classification, whereby HII regions follow the accepted acronyms, N/D indicates a non-detection, U/K indicates where no robust classification could be made, DW indicates a disc-wind, while Jet/DW indicates an ambiguous classification and the presence of an (L) after 'jet' indicates whether lobes were present.

| Object Name	Associated Object	R.A. (J2000)	Dec. (J2000)	D (kpc)	L_{Bol} ($L_\odot$)	5.5 / 9 (GHz)	17 / 22.8 (GHz)	Class.
G010.8411–02.5919⋆	IRAS 18162–2048	$18^h19^m12.09^s$	$-20°47'30.90''$	1.9^a	2.40×10^{4b}	–	E2	Jet
G012.9090–00.2607⋆	IRAS 18117–1753	$18^h14^m39.56^s$	$-17°52'02.30''$	2.4^c	3.20×10^{4a}	–	E3	Jet
G014.9958–00.6732⋆	–	$18^h20^m19.47^s$	$-16°13'29.80''$	2.0^c	1.30×10^{4c}	–	E3	Jet
G251.2337–01.9535	IRAS 08008–3423	$08^h02^m42.97^s$	$-34°31'48.70''$	4.6^a	8.20×10^{3a}	E5	E4	Jet
G254.0491–00.5615	IRAS 08140–3559	$08^h15^m57.12^s$	$-36°08'06.80''$	3.0^a	1.70×10^{3a}	E5	E1	Jet
G254.0548–00.0961	IRAS 08159–3543	$08^h17^m52.62^s$	$-35°52'47.60''$	2.8^a	1.90×10^{3a}	E5	E1	Jet (L)
G263.2283+01.5712	IRAS 08513–4201	$08^h53^m09.46^s$	$-42°13'07.60''$	0.7^d	1.20×10^{3b}	E5	E1	Jet
G263.7434+00.1161	IRAS 08470–4321	$08^h48^m48.64^s$	$-43°32'29.00''$	0.7^d	1.20×10^{3a}	E5	E1	Jet (L)
G263.7759–00.4281	IRAS 08448–4343	$08^h46^m34.84^s$	$-43°54'29.80''$	0.7^d	1.30×10^{3a}	E5	E1	Jet (L)
G265.1438+01.4548	RCW 36	$08^h59^m27.40^s$	$-43°45'03.70''$	0.7^d	7.19×10^{2c}	–	E1,E4	Jet/DW
G268.3957–00.4842	IRAS 09017–4716	$09^h03^m25.08^s$	$-47°28'27.50''$	0.7^d	3.00×10^{3a}	–	E1	N/D
G274.0649–01.1460A	–	$09^h24^m42.54^s$	$-52°01'50.60''$	5.7^a	6.00×10^{3a}	E5	E4	HCHII
G282.2988–00.7769	IRAS 10082–5647	$10^h10^m00.32^s$	$-57°02'07.30''$	3.7^a	4.00×10^{3b}	–	E1	N/D
G283.9146–01.0485	–	$10^h18^m49.96^s$	$-58°10'11.30''$	4.9^a	6.00×10^{3a}	–	E1	N/D
G284.2438–01.1302	IRAS 10187–5810	$10^h20^m35.17^s$	$-58°25'07.10''$	4.2^a	4.40×10^{3a}	E5	E1	CHII
G286.2086+00.1694	IRAS 10365–5803	$10^h38^m32.70^s$	$-58°19'14.30''$	2.3^a	8.00×10^{3a}	–	E1	Jet (L)
G287.3716+00.6444	IRAS 10460–5811	$10^h48^m04.55^s$	$-58°27'01.50''$	4.5^a	1.80×10^{4b}	E5	E1	CHII
G298.2620+00.7394	IRAS 12091–6129	$12^h11^m47.68^s$	$-61°46'18.80''$	4.0^a	1.50×10^{4a}	E5	E3	DW
G300.9674+01.1499†	IRAS 12320–6122	$12^h34^m53.22^s$	$-61°39'40.00''$	4.3^a	4.50×10^{4c}	–	E4	UCHII
G301.1364–00.2249†	IRAS 12326–6245	$12^h35^m35.13^s$	$-63°02'31.60''$	4.3^a	3.80×10^{5a}	–	E3	HCHII
G305.1940–00.0051‡	–	$13^h11^m14.44^s$	$-62°47'25.50''$	4.0^b	7.00×10^{3a}	E5	–	N/D
G305.2017+00.2072A	IRAS 13079–6218	$13^h11^m10.45^s$	$-62°34'38.60''$	4.0^b	3.00×10^{4b}	–	E4	U/K
G305.5610+00.0124	IRAS 13111–6228	$13^h14^m26.36^s$	$-62°44'30.40''$	4.0^b	1.20×10^{4a}	E5	E4	HCHII
G308.9176+00.1231A	IRAS 13395–6153	$13^h43^m01.70^s$	$-62°08'51.20''$	5.3^a	9.00×10^{4a}	–	E4	UCHII
G310.0135+00.3892	IRAS 13481–6124	$13^h51^m37.85^s$	$-61°39'07.50''$	3.2^a	6.70×10^{4a}	E5	E3	Jet (L)
G310.1420+00.7583A	IRAS 13484–6100	$13^h51^m58.27^s$	$-61°15'41.70''$	5.4^a	8.00×10^{3a}	E5	E4	Jet (L)
G313.7654–00.8620‡	IRAS 14212–6131	$14^h25^m01.53^s$	$-61°44'57.60''$	7.8^a	6.10×10^{4a}	E5	–	Jet (L)
G317.4298–00.5612†	IRAS 14477–5947	$14^h51^m37.59^s$	$-60°00'19.40''$	14.2^a	3.50×10^{5a}	E5	–	HCHII
G317.8908–00.0578†	IRAS 14492–5908	$14^h53^m06.16^s$	$-59°02'59.40''$	13.6^a	6.30×10^{4a}	–	E2	UCHII
G318.9480–00.1969A	–	$15^h00^m55.31^s$	$-58°58'52.60''$	2.4^a	1.00×10^{4a}	E5	E3	Jet/DW
G326.6618+00.5207	IRAS 15412–5359	$15^h45^m02.84^s$	$-54°09'03.00''$	1.8^b	1.40×10^{4a}	E5	E2	Jet
G327.1192+00.5103	IRAS 15437–5343	$15^h47^m32.80^s$	$-53°52'39.30''$	4.9^a	3.70×10^{4a}	E5	E2	Jet
G331.3576+01.0626	IRAS 16026–5035	$16^h06^m25.78^s$	$-50°43'22.00''$	4.5^a	1.80×10^{4a}	E5	E3	Jet
G331.5414–00.0675‡	–	$16^h12^m09.00^s$	$-51°25'47.00''$	5.0^a	6.00×10^{4a}	E5	–	UCHII
G332.0939–00.4206	IRAS 16124–5110	$16^h16^m16.46^s$	$-51°18'25.20''$	3.6^b	9.30×10^{4a}	E5	E2	Jet (L)
G332.8256–00.5498A	IRAS 16164–5046	$16^h20^m11.06^s$	$-50°53'16.20''$	3.6^b	1.30×10^{5a}	E5	E2	UCHII
G332.9868–00.4871	RCW 106	$16^h20^m37.81^s$	$-50°43'49.60''$	3.6^b	1.80×10^{4a}	E5	E4	Jet
G337.8442–00.3748†	IRAS 16367–4701	$16^h40^m26.68^s$	$-47°07'13.10''$	3.0^a	3.70×10^{4a}	–	E2	HCHII
G338.9196+00.5495	–	$16^h40^m34.04^s$	$-45°42'07.90''$	4.2^a	3.20×10^{4b}	E5	E3	Jet
G339.6221–00.1209	IRAS 16424–4531	$16^h46^m05.99^s$	$-45°36'43.90''$	2.8^a	1.90×10^{4a}	E5	–	Jet (L)
G339.8838–01.2588	IRAS 16484–4603	$16^h52^m04.66^s$	$-46°08'33.60''$	2.7^a	6.40×10^{4b}	E5	E2	Jet (L)
G340.0543–00.2437A	IRAS 16445–4516	$16^h48^m13.69^s$	$-45°21'42.50''$	3.8^a	2.90×10^{4a}	E5	–	Jet
G340.2480–00.3725†	IRAS 16458–4512	$16^h49^m29.97^s$	$-45°17'44.40''$	3.7^a	3.40×10^{4a}	–	E2	UCHII
G343.1261–00.0623†	IRAS 16547–4247	$16^h58^m17.20^s$	$-42°52'07.10''$	2.8^a	1.90×10^{4a}	–	E2, E4	Jet (L)
G343.5213–00.5171	–	$17^h01^m34.04^s$	$-42°50'19.70''$	3.2^a	6.70×10^{3a}	E5	E4	Jet (L)
G345.4938+01.4677†	IRAS 16562–3959	$16^h59^m41.61^s$	$-40°03'43.30''$	2.4^b	1.50×10^{5b}	–	E2	Jet (L)
G345.5043+00.3480	IRAS 17008–4040	$17^h04^m22.87^s$	$-40°44'23.50''$	2.0^a	1.00×10^{5a}	E5	E4	Jet
G345.9561+00.6123	IRAS 17012–4009	$17^h04^m43.00^s$	$-40°13'13.40''$	2.5^a	2.40×10^{3a}	E5	E3	U/K
G348.6972–01.0263‡	RCW 121	$17^h19^m58.91^s$	$-38°58'14.80''$	2.8^b	1.30×10^{5a}	E5	–	UCHII
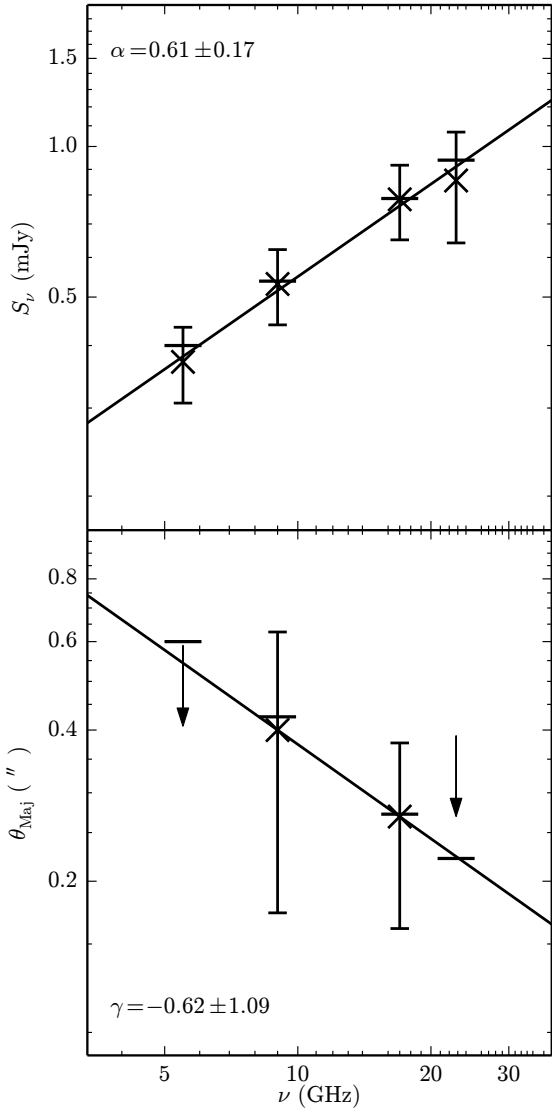
Figure 1. The plotted fluxes (top) and deconvolved major axes (bottom) for both the model (wide horizontal lines) and those recovered through deconvolution with a Gaussian (crosses), for a synthetic dataset. The best fits to the measured fluxes and major axes are shown as black lines. Error bars on the recovered fluxes include a 10% absolute flux-scale uncertainty expected from observations using the ATCA. Upper limits on the recovered major axes are also shown. Model parameters used were, $\alpha = 0.6$, $\gamma = -0.7$, $\theta_{\mathrm{Maj}} = 0.6''$ (major axis at 5.5 GHz) and $\theta_{\mathrm{Min}} = 0.21''$ (minor axis at 5.5 GHz).

The synthetic dataset was created with the use of the miriad task, UVGEN, and mirrors the real observations. Total time on target (positioned at the pointing/phase centres) for the fake observations was 90 minutes, split into five separate 18 minute scans with visibility integration times of 5 seconds. An elevation limit of 30° was imposed (equivalent to a range in hour angle of $-5^{\mathrm{h}} \leqslant$ H.A.$\leqslant 4^{\mathrm{h}}$), and the source declination used ($-60°$) is conservative (for the sample) in terms of the maximum elevations for scans ($< 60°$). Typical values of the system temperature of 30K, 35K, 45K and

100K were used for the 5.5, 9, 17 and 22.8 GHz bands respectively. For the model we used a source with a spectral index $\alpha = 0.6$, a major axis index $\gamma = -0.7$, and a total flux (at 5.5 GHz) of 0.4 mJy. This is representative of a typical ionized wind or jet. The major and minor axes at 5.5 GHz were defined as $0.60''$ and $0.21''$ respectively, corresponding to an opening angle in the jet of 20°.

In Figure 1, we see the model fluxes, the recovered fluxes (through deconvolution with a Gaussian as discussed in §3.3) and the derived spectral index/fit. Flux recovered varied between 91% (at 22.8 GHz) and $>$ 99% (at 17 GHz). A spectral index of 0.61 ± 0.17 was derived, with a derived value for γ of ~ -0.6 (physical sizes could not be deconvolved at 5.5 and 22.8 GHz). This test of the array's performance towards the types of object this paper focusses on, shows that the ATCA effectively recovers the flux and spectral index of a typical ionized jet/wind. The deconvolved sizes were not recovered at both the lower (due to SNR) and upper (due to SNR and the small spatial scales involved) frequencies, while errors were approaching 100% of the deconvolved size at 9 GHz. This shows that for low-SNR objects, the deconvolved dimensions may be unreliable, even though the recovered value for γ in this case is reasonably close to the model's value. Extended sources, such as UCHII regions, will likely not mirror these results.

4   RESULTS

We detect emission in 45 of the 49 fields observed. The maps of radio flux are shown in Figure C1 (online version only) at each observed frequency. For the ionized jets identified (and other associated emission), deconvolved positions are given in Table A1, fluxes/spectral indices are given in Table A2 and sizes/derived values for γ are in Table A3 (these tables are in the online version only). Fluxes, sizes and other derived properties of radio sources identified as HII regions are given in Table A7 (online version only). Any sources that were not part of the sample, but identified within the primary beam of the observations at 5.5 and 9 GHz, have both their fluxes (primary-beam corrected) and positions listed in Table A10 (online version).

4.1   Classification of the radio emission

The major issue concerning the classification of each case is the high degree of similarity between the different types of object (especially at current resolutions). Thus it proved essential to have a classification algorithm to employ on the results reported here. In summary, morphology, radio/bolometric flux comparison, radio spectrum features and correlation with previous observations at different wavelengths form the bulk of this process.

Initially an inspection of the radio emission's morphology is enough to remove UCHIIs (and CHIIs) from the sample. For the more compact radio sources, a comparison of the measured radio fluxes with those expected from the bolometric luminosities (inferred from the models of Davies et al. 2011) aids in the separation of HCHIIs and other types of objects. For this study, a cutoff of 20% of the expected radio flux was used for identification, however other features (such as spectral index or resolving out effects) take precedence over this comparison.

The measurement of radio spectral indices is key to the classification and the models for ionized jets of Reynolds (1986) consequently discriminates between different jet scenarios. Association of the central, thermal component (the jet) with lobes of emission (i.e. a separation of less than 50000 AU and no distinguishable,

infrared counterpart) possessing flat or negative spectral indices is taken as evidence of an ionized jet, with the associated lobes likely representing working surfaces in the outflow cavities or internal shocks in the jet (in the case of non-constant outflow velocity). Deconvolved dimensions and orientations for the thermal components, and comparison with previous studies found in the literature (particularly molecular outflow studies and other signs of outflow) can then help to confirm the ionized jet hypothesis. Disc winds are identified by their characteristic values of $\alpha = 0.6$ and $\gamma = -0.7$, as well a deconvolved position angle for the emission which is perpendicular (more than $45°$) to a previously identified molecular outflow. Should the deconvolved position angle be parallel to the outflow (aligned by less than $45°$), this represents the idealised case of an ionized jet.

4.2 Object results

We report the identification of 28 sources with the characteristics expected of ionized jets, two of which can be identified as either disc-winds or ionized jets (G265.1438+01.4548 and G318.9480-00.1969A). One source (G298.2620+00.7394) is identified as a disc wind. Of the original sample, 14 HII regions (5 HCHII, 7 UCHII and two compact HII regions) have been identified, with 6 other UCHIIs identified in the fields of view for the images. The conditions for classification of the UCHII regions are based on those of Wood & Churchwell (1989). It is also important to note that in cases where there is no clear cut distinction, based upon radius and emission measure, the measured radius of the HII region takes precedence in the classification process.

Four of the sources were not detected at any observing frequency (G268.3957-00.4842, G282.2988-00.7769, G283.9146-01.0485, and G305.1940-00.0051). Figure 2 shows 1 (which was observed at 9 GHz) of the 4 non-detections as a lower-limit, which lies above the flux expected from an ionized jet.

Two objects evaded classification, G305.2017+00.2072A and G345.9561+00.6123. G305.2017+00.2072A imaging displayed evidence of extended, resolved out emission towards the object complicating its deconvolution. Removing shorter baselines did not help to improve the images significantly. Although a faint, compact component was present at 17 GHz coincident with both the MSX point source position and a 6.7 GHz methanol maser, it was not detected at 22.8 GHz and thus no spectral index could be derived. With a bolometric luminosity of $2.4 \times 10^3 L_{\odot}$, G345.9561+00.6123 is one of the less luminous MYSOs in the sample. For the radio emission from an optically thin HII region, a value for $S_{9\text{GHz}}D^2$ (see section 5.1) of 1.6 mJy·kpc^2 is expected for $L_{\text{Bol.}} = 2400 L_{\odot}$, the measured value being (0.56 ± 0.13)mJy·kpc^2 at 9 GHz and (1.75 ± 0.44)mJy·kpc^2 at 17 GHz. Either this may represent an optically thin (at 17 GHz or above), small, emergent HII region or an ionized jet with a large range of possible spectral indices, hence why it remains unclassified.

In summary, the objects reported here have had their classifications tabulated in table 3.

5 ANALYSIS AND DISCUSSION

The analyses presented in this section make use of the Kendall-tau rank correlation test (Kendall 1938) in order to examine the degree of correlation between various observables. It is used on the basis that it is a non-parametric test, making no assumptions of

Table 3. A summary of the numbers and types of objects within the sample, as well as their incidence rate with water masers in the 22.8 GHz band.

Type	Sub-type	Count	Masers?	(%)
Ionized Jet	with lobes	13	6	46
	w/o lobes	13	8	62
Jet/Disc Wind	-	2	1	50
Disc wind	-	1	0	0
HII region	HCHII (embedded)	3	1	33
	HCHII (isolated)	2	1	50
	UCHII	7	5	71
	Compact HII	2	1	50
Unknown	-	2	1	50
Non-detection	-	4	-	-

Table 4. A summary values for the Kendall-Tau coefficient of correlation, the associated p-value, for both the distance-limited (D/L) sample of detected jets and all jets detected (the second column). The size of each sample is tabulated in the third column. τ_{P} represents the partial Kendall-Tau correlation coefficient and the associated p-value (p_{P}), whilst controlling for distance.

(x, y)	S	n	τ	p	τ_{P}	p_{P}
$L_{\text{Bol}}, S_{\nu}D^2$	D/L	22	0.44	0.005	0.32	0.042
	All	28	0.42	0.002	0.35	0.010
$M_{\text{Cl.}}, S_{\nu}D^2$	D/L	15	0.58	0.003	0.47	0.019
	All	17	0.54	0.002	0.49	0.009
$M_{\text{Cl.}}, \dot{M}_{\text{Jet}}$	D/L	15	0.56	0.003	0.55	0.006
	All	18	0.54	0.001	0.53	0.003
$L_{\text{Bol}}, F_{\text{Jet}}$	D/L	21	0.50	0.002	0.46	0.005
	All	25	0.57	< 0.001	0.53	< 0.001

underlying distributions. Results for each of the correlations presented throughout this section are summarised in table 4. For consistency, we initially calculate the Kendall-tau correlation coefficient for measured flux (not distance-flux, $S \cdot D^2$) with distance to be $\tau = 0.18$ with a p-value of 0.38, showing an absence of a Malmquist bias in the distance-limited sample. For fitting the data, we assume a simple power-law and make use of orthogonal distance regression (i.e. total least squares, to account for errors in both independent and dependent variables).

5.1 Radio luminosity vs. bolometric luminosity

Using the parameters of stellar atmospheres reported in Davies et al. (2011) (for $L_{\text{Bol.}} > 10^3 L_{\odot}$), it is possible to infer both the spectral type, and UV photon flux, of a ZAMS star with a specific bolometric luminosity. Since the Lyman flux is intrinsically associated with the amount of material which a young protostar can ionize, we can infer the (optically thin) radio continuum flux expected from an optically thin HII region produced by such a UV flux. Therefore, using this expected radio flux from the bolometric luminosities of the objects, can help to distinguish between HII regions and less evolved phases of massive star formation. The specific radio luminosity expected for ionized jets and winds is not as easy to constrain, due to a lack of theoretical models which incorporate all the variables likely influencing the radio luminosity of jets. Therefore, in order to provide us with an idea of the fluxes expected of these objects, we look towards the empirical relations of radio luminosity against bolometric luminosity, $S_{\nu}D^2 \simeq 10^{-2.1} L_{\text{Bol}}^{0.6}$, derived by Anglada (1995). As this relation is derived from a low-
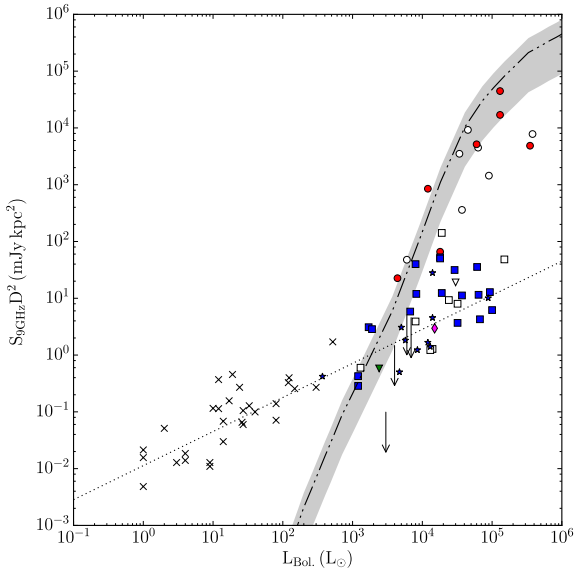
Figure 2. A plot of the 9 GHz distance-luminosities against bolometric luminosity for all detected objects (apart from non-thermal lobes) in the sample. Circles (red) represent HII regions, squares (blue) represent ionized jets, diamonds (magenta) represent those sources displaying disc-wind characteristics, triangles (green) represent objects of unknown classification and crosses mark low-mass cases normalized to 9 GHz (assuming $\alpha = 0.6$), from Anglada (1995). Filled (coloured online) symbols show cases where the flux has been directly measured at 9GHz, while hollow symbols show cases where the flux has been interpolated from measured spectral indices and higher frequency observations. The star symbols represent the sample of jets from Moscadelli et al. (2016). Lower limits ($< 3\sigma$) of non-detections are shown. The dot-dashed line represents the ionized flux expected from the Lyman continuum, taken from stellar models by Davies et al. (2011) for $L_{Bol.} > 10^3 L_\odot$, and Thompson (1984) for $L_{Bol.} \leqslant 10^3 L_\odot$. Grey shading represents the area where the radio-luminosity is between $20 - 180\%$ of that expected from the bolometric luminosity (for a HII region). The dotted line represents the empirical relation derived for the low-mass case (Anglada 1995), normalized to 9GHz (assuming $\alpha = 0.6$).

mass sample with a maximum bolometric luminosity of $\sim 500 L_\odot$ it serves as a comparison for the fluxes we expect to see for thermal jets from MYSOs. Should the mechanism for ionization/jet production be different to the models of shock-ionization (Curiel et al. 1987), we should expect to see a deviation towards the higher masses of the MYSOs.

Figure 2 shows structure attributable to the clear divide between the bright, HII regions near the expected Lyman-continuum line and the jet-like objects which are not as bright as expected from their bolometric luminosities. The HII regions which occupy radio luminosities similar to those of the jets are either resolved out extended regions (higher bolometric luminosities), or are small HCHII regions around lower bolometric luminosity MYSOs. Distinguishing between these two possibilities then falls to infrared observations and previously reported signatures of jet activity. It is worth noting that we expect to see lower radio luminosities for the HII regions than expected from the models of Davies et al. (2011), due to significant dust absorption of Lyman continuum photons (Wood et al. 1988).

The jets themselves can be fitted with a power-law with an in-

dex of 0.97±0.20 ($\tau = 0.47$, p-value= 0.001), greater than that seen for the low-mass case of 0.6. We must add that fitting the low-mass jet sample of Anglada (1995) with the same algorithms as employed upon our high-mass sample yields a higher coefficient of 0.67 ± 0.10 ($\tau = 0.55$, p-value= 3×10^{-5}). When fitting both the high-mass and low-mass sample of jets together, we arrive at a coefficient value of 0.77±0.02 ($\tau = 0.995$, p-value~ 0). This may imply that either different processes are required to explain the ionization within the high-mass jets, or that there is more ionized material around the MYSOs other than that of the collimated jet. This material may present itself as a small ionized core at small radii around the MYSO (which is part of the models of Reynolds 1986), existing with the collimated jet contemporaneously, although higher resolution observations would be required to determine this (sub-milliarcsecond for 15 AU at a distance of 3 kpc).

Of the 34 MYSOs from which the distance-limited sample is comprised, we detect a total of 20 jets, of which 10 are associated with radio lobes. The mean (and its standard error) bolometric luminosities of isolated jets and jets with lobes are $(2.6 \pm 0.9) \times 10^4 L_\odot$ and $(2.7 \pm 1.0) \times 10^4 L_\odot$ with medians of $1.8 \times 10^4 L_\odot$ and $8.0 \times 10^3 L_\odot$ respectively, showing only small differences between the two populations in this respect.

5.2   9GHz Luminosity vs. Clump Mass

An ATLASGAL survey by Urquhart et al. (2014), recorded the 870µm fluxes and sizes of a sample of clumps, 35 of which coincide with sources in this survey. We define the term 'clump' as being the substructure within giant molecular clouds (GMCs) which ultimately evolve into stellar clusters. In turn, they harbour the smaller substructure of 'cores', which are defined as the evolutionary precursor of single (which may or may not display multiplicity) stellar systems (Zinnecker & Yorke 2007). Of those 35 sources, 21 have been classified as exhibiting jet-like characteristics. The clump mass was therefore inferred using the referenced dataset in conjunction with the equations of Hildebrand (1983).

In Figure 3 the radio luminosities at 9GHz have been plotted against the calculated clump masses and a relation of $S_\nu D^2 \propto M_{clump}^{1.57 \pm 0.31}$ is derived. Two outliers toward the heavier end of the clump masses are identified in figure 3 by annotation. G014.9958–00.6732 suffered from elongated beams and noisier data as a result of its observed times. G338.9196+00.5495 is known to be in an extremely active star formation region in general, as well as being located at the edge of its natal clump (see §5.5).

Neglecting the two outliers (and G012.9090–00.2607 for the same justification as for G014.9958–00.6732), we calculate the correlation coefficient between the clump masses and distance fluxes at 9GHz (for the distance-limited sample, neglecting G338.9196+00.5495 and G014.9958–00.6732) to be $\tau = 0.54$ with a p-value of 0.002, for our jet sample. This indicates a high likelihood of a positive correlation between the two quantities and justifies the empirical power-law, fitted in Figure 3. For the partial Kendall correlation coefficient for distance-flux with clump mass (controlling for distance) we calculate a value of $\tau = 0.49$ with a p-value of 0.008. This statistical result again supports the correlation between jet luminosity and clump mass, as well as the fact that the most massive stars form in the most massive clumps.
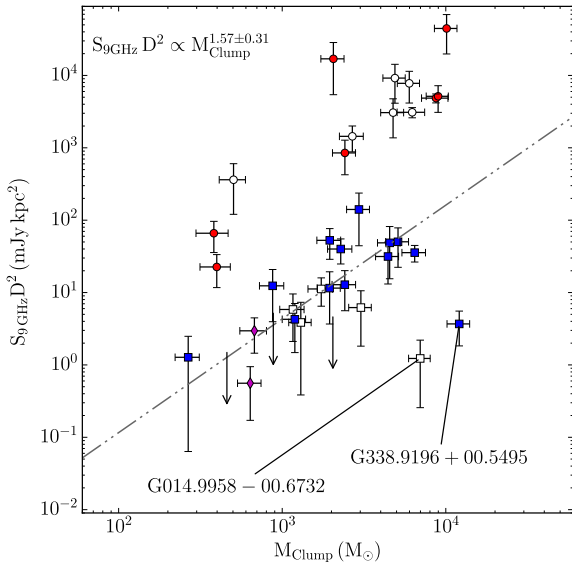
Figure 3. A plot of the 9GHz distance fluxes against associated clump masses for HII regions and objects displaying properties associated with either ionized jets or disc winds. The coefficient to the fitted power-law fit is displayed in the top left corner and is represented as the dot-dashed line. Symbols have the same meanings as in Figure 2.

Figure 4. A plot of the logarithm of the 9GHz fluxes against the MSX 8μm/21μm colour for the nearest associated MSX point source, for the HII regions and ionized jets detected. Symbols follow the conventions of Figure 2

5.3 Radio luminosity vs. IR colours

As discussed in §2.1, the reddening of sources in infrared surveys can be an accurate indicator of youth since the greater the degree of reddening, the more embedded a source will be in its environment. Extrapolating this reasoning to the MYSO phase, the radio luminosity at 9 GHz has been plotted against the MSX (21μm-8μm) colour in Figure 4.

While the HII regions appear to show higher radio luminosities with the more reddened mid-infrared colours, the jets show no correlation, holding similar fluxes over the sampled colour-space. This may indicate that the jet phase occupies a relatively large portion of an MYSO's lifetime. Non-detections occupy the same range of colours as the detected jets themselves. Considering the average bolometric luminosities for the detections and non-detections of the sample are $3.7 \times 10^4 L_\odot$ and $3.7 \times 10^3 L_\odot$ respectively, the signal to noise ratio may be insufficient to detect any free-free emission, should it exist coincident with the MSX sources with no detected radio flux. It is also interesting to note that the sources exhibiting disc-wind properties occupy a wide range of colours. However, of these, the unambiguous disc wind (G298.2620+00.7394) holds one of the reddest colours of the jets/disc-winds in the sample. Definite conclusions about whether disc winds represent separate evolutionary stages in MYSO evolution would require a larger sample of such objects than that presented in this work.

5.4 Coincidence with maser and line emission

With regards to the water maser line at 22.23508 GHz, we detect emission within $10''$ of 22 of the 42 sources observed in the 22.8 GHz band. Two more of the 42 sources have a detection of water maser activity in previous studies (Forster & Caswell 1999), making a total of 24 of 42 sources. The exact breakdown in terms of object type is summarised in table 3.
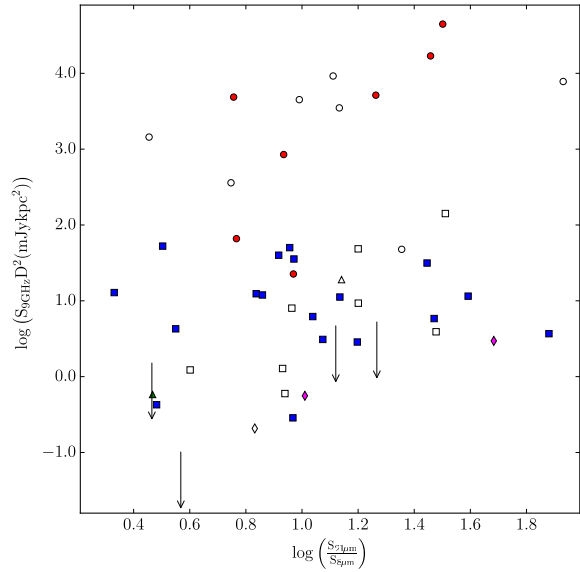
In comparison with the survey by Urquhart et al. (2009), we find a detection rate of 52% compared to their rate of 27%. This is likely due to the SNR ($\sim$ 50 times lower) of this survey since it is continuum oriented (i.e. 1 MHz channels), compared to the previous line oriented study ($4\sigma \sim$ 1Jy). Given the (spectrally) low-resolution nature of continuum observations, no kinematic information could be derived.

5.5 Ionized jets and their general properties

Using equation 5 (Reynolds 1986), it is possible to infer a mass loss rate in the jet:

$$\dot{M}_{\mathrm{Jet}} = \frac{9.38 \times 10^{-6} \, v_8 \, \mu \, S_{\mathrm{mJy}}^{3/4} \, d_{\mathrm{kpc}}^{3/2} \, \theta_0^{3/4}}{x_0 \, \nu_{10}^\alpha \, \nu_{m10}^{0.45 - \frac{3\alpha}{4}} \, T_4^{0.075} \, (\sin i)^{1/4} \, F^{3/4}} \tag{5}$$

where α is the derived spectral index, μ is the average particle mass (as a fraction of the proton mass), x_o is the ionization fraction, v_8 is the terminal velocity of the jet (assumed to be $500 \, \mathrm{km \, s^{-1}}$ from proper motion studies in the literature), S_ν is the integrated flux density, D is the distance to the source, ν_{m10} is the turnover frequency, i is the inclination angle (assumed to be $\sim 39°$), T is the electron temperature and θ_0 is the opening angle at the base of the jet, in radians ($\theta_0 = 2 \tan^{-1}(\theta_{\mathrm{min}}/\theta_{\mathrm{maj}})$). F is given below in equation 6:

$$F \equiv F(q_\tau, \alpha) \equiv \frac{4.41}{q_\tau (\alpha - 2)(\alpha + 0.1)} \tag{6}$$

where q_τ is the power-law coefficient with which the opacity falls with distance along the jet propagation axis.

Equations 5 and 6 necessitate us to make assumptions for the non-observable parameters contained within them. We assume a higher ionization fraction than in the low-mass case ($\sim$ 0.1 Hartigan et al. 1994) of 0.2, a typical jet velocity of 500 km s^{-1}, (as

seen in §1 for other examples of ionized jets around MYSOs) and an electron temperature of 10000 K. For the inclination angle, a value of $39.54°$ is adopted since the average value for $\sin(i)$ (for uniformly distributed, random inclinations) is found to be ~ 0.64. These values are used for all of the jets in the sample. The turnover frequency is assumed to be 50 GHz, apart from for the jets whereby $\alpha < 0$, in which case we are already in the optically thin regime and the lowest observed frequency is used. The highest (i.e most resolving) frequency measurements of the minor/major axes are used in the calculation of the opening angle, for which we find a range between $17 - 80°$ and an average value of $\sim 40°$, higher than the range of opening angles found by Moscadelli et al. (2016) towards their sample of MYSOs, and much greater than typical low-mass cases ($5 - 10°$ Tsinganos et al. 2009). The widest opening angle was found towards G313.7654−00.8620, which represents a morphologically complex MYSO in the radio, which may affect the deconvolution (which is reflected in opening angle errors of $42°$).

A more complex approach is used when assuming values for q_τ. Since (from Equation 1) it is dependent on values for ϵ and q_T, we assume one of three models. In the case of $0.4 \leqslant \alpha < 0.8$, we assume $\epsilon = 1$ and $q_\mathrm{T} = 0$, the "standard" spherical model. Where α is measured to be less than 0.4, we assume $\epsilon = 2/3$ and $q_\mathrm{T} = 0$, the "standard" collimated model. Finally, in the instances where $\alpha \geqslant 0.8$, we assign values of $\epsilon = 1$ and $q_\mathrm{T} = -0.5$, a conical, recombining jet model.

We calculate an average mass loss rate of $2.7 \times 10^{-5} \mathrm{M}_\odot \mathrm{yr}^{-1}$ across all detected jets. Plotting the derived mass loss rates against the clump masses (Figure 5) shows a power law with an index of 1.28 ± 0.31. For this correlation we calculate $\tau = 0.562$ with an associated p-value of ~ 0.003, for those objects comprising the distance limited sample. For all the jets in the sample, we calculated $\tau = 0.542$ and a p-value of 0.001. As shown in table 4, these values do not appreciably change for the partial correlation coefficients, whilst controlling for distance. This confirms that the mass loss rates in the jets are related to the clump masses, without a distance related bias.

Three jets were neglected from the plots (G012.9090–00.2607, G014.9958–00.6732 and G338.9196+00.5495). W33A (G012.9090–00.2067) and the Kleinmann-Wright (Kleinmann & Wright 1973) object (G014.9958.00-6732) both lie at declinations conducive to elongated beam shapes, thus adversely affecting their deconvolved sizes. Indeed, W33A was found to have a deconvolved size of $(0.53'' \pm 0.14) \times (0.27'' \pm 0.11)$ at 43GHz by van der Tak & Menten (2005), giving an opening angle at the base of the jet of 0.94 rads, in contrast to our derived value of 0.18 rads. This would in turn derive $\dot{\mathrm{M}}_\mathrm{jet} = (1.7 \pm 1.0) \times 10^{-5} \mathrm{M}_\odot \mathrm{yr}^{-1}$ (our derived value is $(5.0 \pm 3.2) \times 10^{-6} \mathrm{M}_\odot \mathrm{yr}^{-1}$). W33A is also known to be composed of at least 3 separate sources at very high resolutions, Q1, Q2 and Q3 (Q1 represents the main jet). This complicates the analysis, requiring higher resolutions observations at all frequencies in order to separate and determine the natures of each source.

The KW object is positioned at the edges of two ATLASGAL ($\mathrm{R}_\mathrm{eff} \sim 60''$ and $\mathrm{R}_\mathrm{eff} \sim 90''$) clumps, the membership to which is uncertain. If the accretion, and hence jet mass loss rates, are intrinsically tied to the reservoir of material from the clump, this may explain (in combination with the elongated beam) its current (relatively low) mass loss rate of $\sim 4 \times 10^{-6} \mathrm{M}_\odot \mathrm{yr}^{-1}$.

G338.9196+00.5495 images had low signal to noise ratios, showed the presence of 5 HCHII/UCHIIs within $1'$ of the source, and displayed partially resolved out extended emission at the lowest frequencies. The busy nature of the environment would affect the reservoir of available material to the MYSO and hence af-
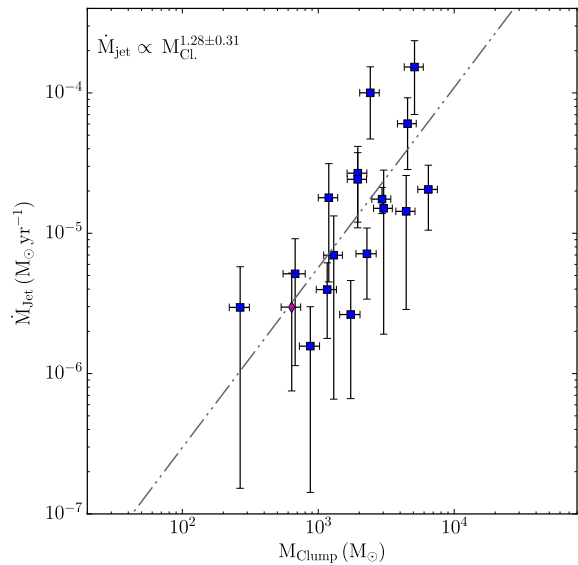

Figure 5. A plot of the inferred mass loss rates against ATLASGAL derived clump masses (Urquhart et al. 2014) in the jet for all the sources in our sample displaying jet-like characteristics. The dot-dashed line represents the power-law fit to the data, with the power-law index indicated in the top left of the plot.

fect jet outflow rates, as well as the quality of the images and deconvolved dimensions of the object itself (which is unresolved at 17 and 22.8GHz). ATLASGAL images of G338.9196+00.5495 also show its parental clump to be comprised of two, non-resolved clumps, with the source offset on the southern edge of the smaller, thus the clump's mass may be overestimated. Considering that G338.9196+00.5495 is also an outlier in Figure 3, it is likely that the clump mass is poorly constrained as discussed above.

As a check with the rest of the data, all sources apart from the KW object, G338.9196+00.5495 and G345.9561+00.6123 (which is still of uncertain classification) are positioned within the inner 25% of their parental clumps (c.f. Urquhart et al. 2014, who found 90% of embedded objects were separated by less than 0.5pc from their associated clump's peak flux position).

Inferred momentum rates of the jets (assuming a terminal velocity for the jet of $500 \mathrm{km\,s}^{-1}$) against the bolometric luminosities of the powering sources, are plotted in Figure 6. We find the relation presented in equation 7. Comparing this to the CO outflow momentum rate/bolometric luminosity relations found by Cabrit & Bertout (1992) (equation 8) and Maud et al. (2015) (equation 9):

$$\log_{10} \mathrm{F}_\mathrm{jet} = (-6.33 \pm 0.60) + (1.00 \pm 0.14) \log_{10} \mathrm{L}_\mathrm{bol} \quad (7)$$

$$\log_{10} \mathrm{F}_\mathrm{CO} = (-4.36 \pm 0.12) + (0.69 \pm 0.05) \log_{10} \mathrm{L}_\mathrm{bol} \quad (8)$$

$$\log_{10} \mathrm{F}_\mathrm{CO} = (-4.60 \pm 0.46) + (0.61 \pm 0.11) \log_{10} \mathrm{L}_\mathrm{bol} \quad (9)$$

Within errors, the momentum rate of ionized jets appears to depend more heavily on the bolometric luminosities than the molecular outflows. However the incidence rate of massive molecular outflows in the (6kpc distance-limited) MYSO sample of Maud et al. (2015) was found to be 66%, similar to the incidence rate of jets for our distance-limited sample of 59%. The power-law coeffi-
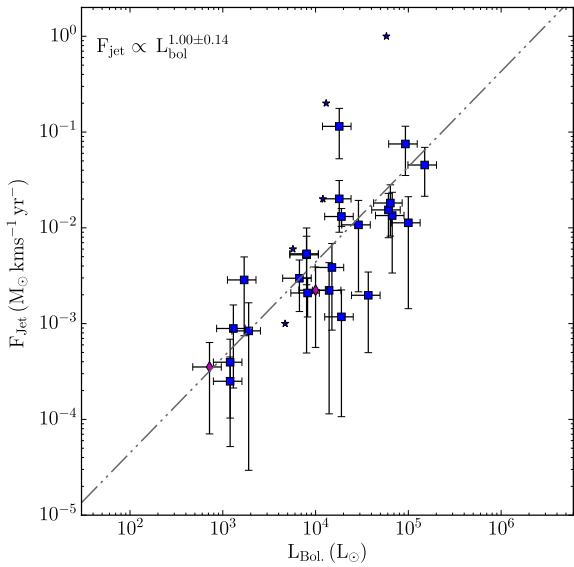
Figure 6. A plot of the inferred momentum rate against bolometric luminosity for the sources in our sample displaying jet-like characteristics. The dot-dashed line represents the power-law fit to the data, with the power-law index indicated in the top left of the plot.
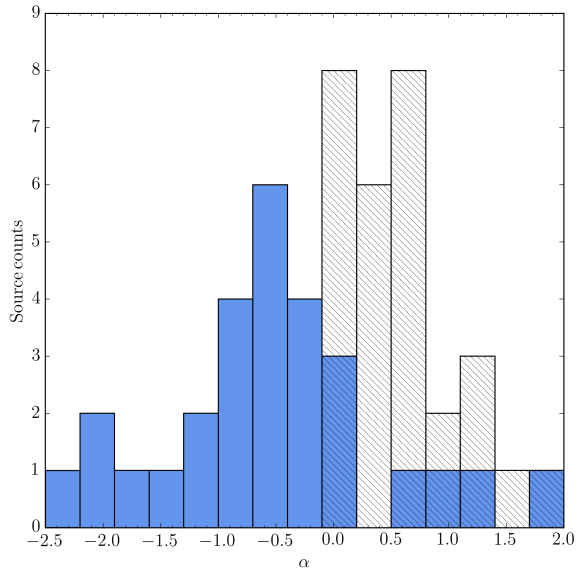

Figure 7. A histogram of all the spectral indices derived for those sources determined to exhibit jet-like characteristics (hatched). The solid blue bars are for the associated lobes. Binning starts at $\alpha = -2.5$ and bin widths are set at 0.3 due to the sample size.

cient for the relation between the molecular mass outflow rate and clump mass was found to be 0.55 ± 0.10. In comparison to our fitted value of 1.28 ± 0.31 for the jet outflow rate, this indicates a heavier dependence of the outflow rates on the clump mass for ionized jets, than for the molecular outflows.

In Figure 7, the histogram of the spectral indices derived for all jets in our sample is presented. This shows a greater number of jets showing optically thinner spectral indices, with spectral indices peaking between -0.1 and 0.3 in our sample. All detected jets exhibit spectral indices expected from the models of Reynolds (1986) of between -0.1 and 1.6 (within errors). As for the lobes of emission associated to the thermal jets, we derive non-thermal spectral indices for lobes associated to 10 of the 13 jets. An average spectral index in the non-thermal lobes of -0.53 is also calculated showing that synchrotron emission is the dominant emission mechanism in these cases and therefore magnetic fields are present in the immediate environments of ionized jets from MYSOs. Four of the jets show associated lobes with thermal spectral indices, G310.0135+00.3892 (SW), G310.1420+00.7583A (B), G313.7654-00.8620 (B2) and G332.0939-00.4206 (E). For all four cases, apart from G313.7654-00.8620, the spectra of the components are not well fitted by simple power-laws suggesting these components represent extended emission (i.e. resolved out at higher frequencies), the natures of which are indeterminate. G313.7654-00.8620 was observed at the lower two frequencies only, and so the presence of this effect is unknown, raising another possibility of multiplicity.

For those jets identified which had associated lobes of emission, the separation of these lobes from the central jet was calculated (assuming an inclination of $90°$) and in Figure 8, the histogram of logarithmic lobe separations is plotted. A peak in the separations at $\sim 10^4 \mathrm{AU}$ from the central object is evident, with a mean value of $2.0 \times 10^4 \mathrm{AU}$ (and a median value of $1.3 \times 10^4 \mathrm{AU}$). The minimum separation calculated ($\sim 6 \times 10^4 \mathrm{AU}$) was for

the NW component of G263.7759–00.4281, while the maximum ($\sim 9 \times 10^4 \mathrm{AU}$) was for component D of G313.7654–00.8620. If these lobes represent internal shocks within the jet as a result of periodic ejection coupled with non-constant ejection velocities we can calculate the typical time between these ejections. Assuming an ejection velocity of $500 \mathrm{km\,s^{-1}}$ for the first ejection, which increases by 10% for the second, and using the typical value for lobe separations of $1.3 \times 10^4 \mathrm{AU}$, it can be inferred that the time between these ejections is typically $\sim 10 \mathrm{years}$.

It is important to note that the population of small separation lobes is under-sampled and we cannot reliably comment on lobe separations for distances $< 4000 \mathrm{AU}$, due to the minimum resolvable scales of the observations. In order to investigate the spectral consequences of this resolution limit, we analysed the spectral indices for the combined fluxes of north and south lobes, for both G263.7434+00.1161 and G310.0135+00.3892 (due to their relative morphological simplicities). Derived values for the spectral index of the combined emission were found to be $\alpha = 0.09 \pm 0.13$ and $\alpha = 0.42 \pm 0.17$ for G263.7434+00.1161 and G310.0135+00.3892 (for the thermal jets alone, $\alpha = 0.39 \pm 0.18$ and $\alpha = 1.27 \pm 0.18$) respectively, with the combined fluxes being fitted well with a simple power law. This indicates that any unresolved, optically thin lobes which are inseparable from their powering, thermal jets, would flatten the jet's spectrum without strongly distorting its power law profile. This effect could act to decrease the measured spectral index for jets, whose flux incorporates those of optically thin or non-thermal lobes, offering another explanation for the large proportion of jets with spectral indices between -0.1 and 0.3 (see Figure 7).

5.6 HII regions and their general properties

From the HII regions that were included in the overall sample, we have calculated both the emission measures and physical radii (de-
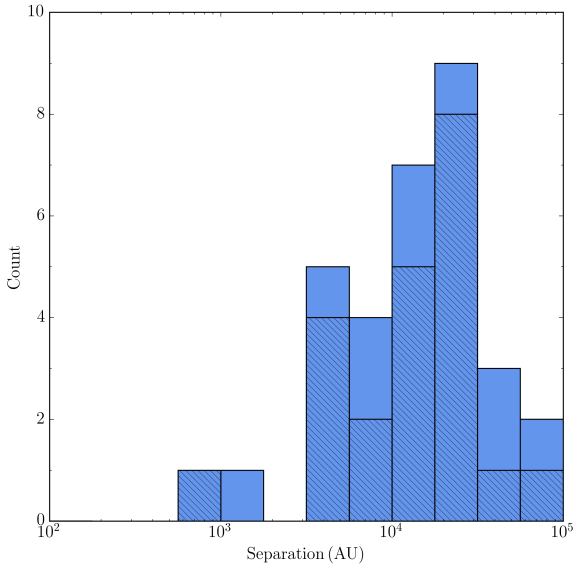
Figure 8. A logarithmic histogram of the spatial separations between all lobes (solid bars), and lobes where $\alpha < 0$ (hatched bars), and their powering central jets.

convolved). The three HCHII regions displaying a compact core have been separated from their extended background emission, with both components analysed separately. Both emission measures and radii are plotted in Figure 9.

For the HCHII regions in our sample, we find an average emission measure of $6.51 \times 10^8 \, \mathrm{pc \, cm^{-6}}$ and corresponding electron density of $2.28 \times 10^5 \, \mathrm{cm^{-3}}$. For the ultra-compact HII regions detected, we find values of $1.09 \times 10^8 \, \mathrm{pc \, cm^{-6}}$ and $5.13 \times 10^4 \, \mathrm{cm^{-3}}$ for the average emission measure and electron density. Average radii were calculated to be 0.013pc and 0.041pc, while average bolometric luminosities were calculated to be $(1.6 \pm 0.4) \times 10^5 \, \mathrm{L_\odot}$ and $(7.9 \pm 1.1) \times 10^4 \, \mathrm{L_\odot}$, for HCHIIs and UCHIIs respectively (assuming a 34% error in the bolometric luminosities, as in Mottram et al. 2011). Although HII regions are not the focus of this paper, the derived properties provide a consistency check for typical values reported in the literature (Mezger et al. 1967; Wood & Churchwell 1989; Hoare et al. 2007).

6 CONCLUSIONS

In this work, we present the results of radio observations made towards 49 massive young stellar objects potentially harbouring ionized jets, 34 of which form a distance-limited sample . Our goal is to establish how common this phenomenon is for the formation process of massive stars, the relation to possible accretion processes/models and the physical parameters typical of the jets themselves. In summary, our main results and conclusions are:

(i) From the distance-limited sample of 34 MYSOs we detect 20 ionized jets (excluding two potential disc winds) showing this to be a common phenomenon in forming massive stars. Disc based accretion processes are therefore the dominant mechanism of accretion (up to masses of at least $25 \mathrm{M_\odot}$).

(ii) Ionized jets are more common than disc winds, by at least an order of magnitude. This suggests that either ionized jets are
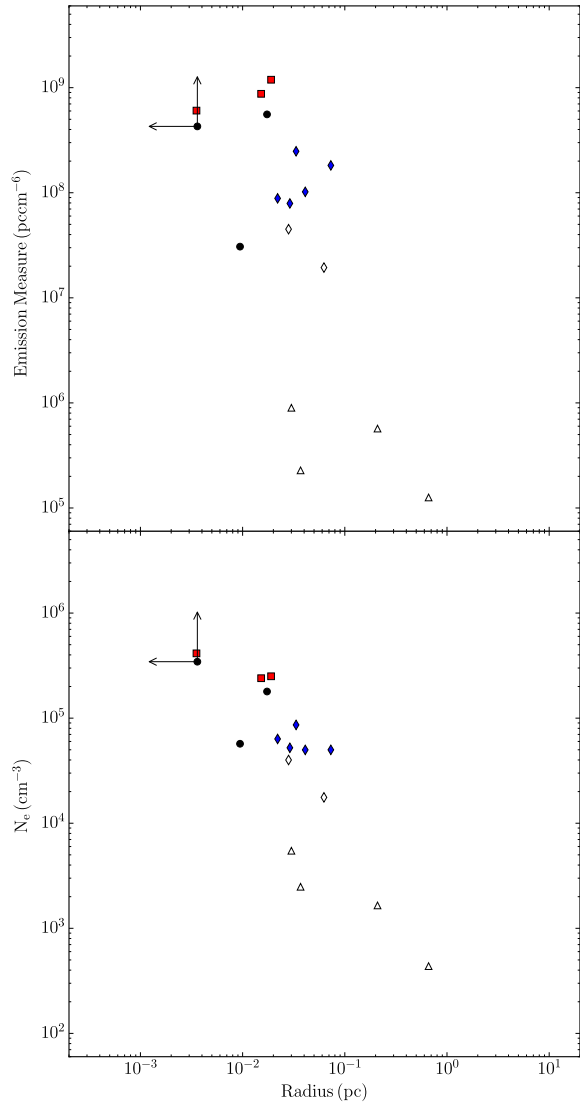

Figure 9. A plot of the calculated emission measures against radius for the HII regions detected in our sample (top) and the corresponding electron densities inferred against radius (bottom). Circles (black) represent the compact HCHII 'core' seen in 3 HII regions, squares (red) represent other HCHII regions, diamonds (blue) represent UCHII regions, and triangles represent compact and classical HII regions. Any symbols in white suffer from resolving out effects due to their scale.

generally brighter than disc winds (if they are concurrent), or that a distinct disc-wind phase exists and is relatively short in comparison.

(iii) Assuming a MYSO phase lifetime of $\sim 10^5 \mathrm{yr}$ (McKee & Tan 2002), a jet-phase lasting $(5.9 - 6.5) \times 10^4 \mathrm{yr}$ is implied from the incidence rate. Since some objects potentially represent a transition phase between ionized jet and HII region, this time range is placed at the later end of an MYSO's lifetime, implying accretion doesn't completely halt after the initial production of an HII region.

(iv) The luminosity of our sample of massive, ionized jets scales with bolometric luminosity in the same way (within errors) as low-

mass jets, supporting the idea that these jets are produced in the same way over YSO mass ranges upto at least $25M_\odot$.

(v) Typical jet mass-loss rates and momenta rates are $2.7 \times 10^{-5} M_\odot \, \mathrm{yr}^{-1}$ and $1.4 \times 10^{-2} M_\odot \, \mathrm{km \, s}^{-1} \mathrm{yr}^{-1}$ respectively, assuming an average ionization fraction of 20% and jet velocity of $500 \mathrm{km \, s}^{-1}$. This suggests an average mass of $\sim 2M_\odot$ (corresponding to $\sim 10^{43}$ ergs) is lost through the ionized jet mechanism, to the ISM, over the course of an MYSOs jet-phase.

(vi) Jet outflow rates (and hence accretion rates) are closely related to the mass of the molecular clump from which they form, which agrees with the idea that the most massive stars form in the most massive clumps. This is also supported by the fact that 88% of the jets are found in the inner 25% of their associated clump.

(vii) Synchrotron emission is commonplace (present in $\sim 75\%$ of the jets displaying associated lobes) and as a result, this lends support to the idea of magnetic collimation in ionized jets around MYSOs, as in the low mass case.

REFERENCES

Anglada G., 1995, in Lizano S., Torrelles J. M., eds, Revista Mexicana de Astronomia y Astrofisica Conference Series Vol. 1 of Revista Mexicana de Astronomia y Astrofisica, vol. 27, Centimeter Continuum Emission from Outflow Sources. p. 67

Arce H. G., Shepherd D., Gueth F., Lee C.-F., Bachiller R., Rosen A., Beuther H., 2007, PPV, pp 245–260

Beuther H., Schilke P., Sridharan T. K., Menten K. M., Walmsley C. M., Wyrowski F., 2002, A&A, 383, 892

Blandford R. D., Payne D. G., 1982, MNRAS, 199, 883

Bonnell I. A., Bate M. R., Clarke C. J., Pringle J. E., 2001a, MNRAS

Bonnell I. A., Clarke C. J., Bate M. R., Pringle J. E., 2001b, MNRAS

Bronfman L., Nyman L.-A., May J., 1996, A&AS, 115, 81

Burkert A., Stecklum B., Henning T., Fischer O., 2000, A&A, 353, 153

Cabrit S., Bertout C., 1992, A&A, 261, 274

Campbell B., 1984, ApJ, 282, L27

Caratti o Garatti A., Stecklum B., Linz H., Garcia Lopez R., Sanna A., 2015, A&A, 573, A82

Carrasco-González C., Galván-Madrid R., Anglada G., Osorio M., D'Alessio P., Hofner P., Rodrguez L. F., Linz H., Araya E. D., 2012, The ApJ Journal Letters, 752, L29

Caswell J. L., 1998, MNRAS, 297, 215

Caswell J. L., Fuller G. A., Green J. A., Avison A., Breen S. L., Ellingsen S. P., Gray M. D., Pestalozzi M. R., Quinn L., Thompson M. A., Voronkov M. A., 2011, MNRAS, 417, 1964

Curiel S., Canto J., Rodriguez L. F., 1987, RMxAA, 14, 595

Curiel S., Ho P. T. P., Patel N. A., Torrelles J. M., Rodríguez L. F., Trinidad M. A., Cantó J., Hernández L., Gómez J. F., Garay G., Anglada G., 2006, ApJ, 638, 878

Cyganowski C. J., Whitney B. A., Holden E., Braden E., Brogan C. L., Churchwell E., Indebetouw R., Watson D. F., Babler B. L., Benjamin R., Gomez M., Meade M. R., Povich M. S., Robitaille T. P., Watson C., 2008, ApJ, 136, 2391

Davies B., Hoare M. G., Lumsden S. L., Hosokawa T., Oudmaijer R. D., Urquhart J. S., Mottram J. C., Stead J., 2011, MNRAS, 416, 972

De Buizer J. M., Walsh A. J., Piña R. K., Phillips C. J., Telesco C. M., 2002, ApJ, 564, 327

de Luca M., Giannini T., Lorenzetti D., Massi F., Elia D., Nisini B., 2007, A&A, 474, 863

Eisloffel J., Mundt R., Ray T. P., Rodriguez L. F., 2000, Protostars and Planets IV, pp 815–840

Ellingsen S. P., Norris R. P., McCulloch P. M., 1996, MNRAS, 279, 101

Faúndez S., Bronfman L., Garay G., Chini R., Nyman L., May J., 2004, A&A, 426, 97

Forster J. R., Caswell J. L., 1999, A&AS, 137, 43

Frater R. H., Brooks J. W., Whiteoak J. B., 1992, Journal of Electrical and Electronics Engineering Australia, 12, 103

Garay G., Mardones D., Bronfman L., Brooks K. J., Rodríguez L. F., Güsten R., Nyman L.-Å., Franco-Hernández R., Moran J. M., 2007, A&A, 463, 217

Gibb A. G., Hoare M. G., 2007, MNRAS, 380, 246

Green J. A., Caswell J. L., Fuller G. A., Avison A., Breen S. L., Ellingsen S. P., Gray M. D., Pestalozzi M., Quinn L., Thompson M. A., Voronkov M. A., 2012, MNRAS, 420, 3108

Guzmán A. E., Garay G., Brooks K. J., 2010, ApJ, 725, 734

Guzmán A. E., Garay G., Brooks K. J., Voronkov M. A., 2012, ApJ, 753, 51

Guzmán A. E., Garay G., Rodríguez L. F., Moran J., Brooks K. J., Bronfman L., Nyman L.-Å., Sanhueza P., Mardones D., 2014, ApJ, 796, 117

Hartigan P., Morse J. A., Raymond J., 1994, ApJ, 436, 125

Henning T., Lapinov A., Schreyer K., Stecklum B., Zinchenko I., 2000, A&A, 364, 613

Henning T., Schreyer K., Launhardt R., Burkert A., 2000, A&A, 353, 211

Higuchi A. E., Saigo K., Chibueze J. O., Sanhueza P., Takakuwa S., Garay G., 2015, ApJ, 798, L33

Hildebrand R. H., 1983, QJRAS, 24, 267

Hoare M. G., Kurtz S. E., Lizano S., Keto E., Hofner P., 2007, Protostars and Planets V, pp 181–196

Hosokawa T., Omukai K., 2009, ApJ, 691, 823

Ilee J. D., Wheelwright H. E., Oudmaijer R. D., de Wit W. J., Maud L. T., Hoare M. G., Lumsden S. L., Moore T. J. T., Urquhart J. S., Mottram J. C., 2013, MNRAS, 429, 2960

Kendall M. G., 1938, Biometrika, 30, 81

Kleinmann D. E., Wright E. L., 1973, ApJ, 185, L131

Kraus S., Hofmann K.-H., Menten K. M., Schertl D., Weigelt G., Wyrowski F., Meilland A., Perraut K., Petrov R., Robbe-Dubois S., Schilke P., Testi L., 2010, Nature, 466, 339

Lizano S., 2008, in Beuther H., Linz H., Henning T., eds, Massive Star Formation: Observations Confront Theory Vol. 387 of Astronomical Society of the Pacific Conference Series, Hypercompact HII Regions. p. 232

Lumsden S. L., Hoare M. G., Oudmaijer R. D., Richards D., 2002, MNRAS, 336, 621

Lumsden S. L., Hoare M. G., Urquhart J. S., Oudmaijer R. D., Davies B., Mottram J. C., Cooper H. D. B., Moore T. J. T., 2013, ApJS, 208, 11

Marti J., Rodriguez L. F., Reipurth B., 1993, ApJ, 416, 208

Martí J., Rodríguez L. F., Reipurth B., 1998, ApJ, 502, 337

Massi F., de Luca M., Elia D., Giannini T., Lorenzetti D., Nisini B., 2007, A&A, 466, 1013

Maud L. T., Moore T. J. T., Lumsden S. L., Mottram J. C., Urquhart J. S., Hoare M. G., 2015, MNRAS, 453, 645

McKee C. F., Tan J. C., 2002, Nature, 416, 59

McMullin J. P., Waters B., Schiebel D., Young W., Golap K., 2007, in Shaw R. A., Hill F., Bell D. J., eds, Astronomical Data Analysis Software and Systems XVI Vol. 376 of Astronomical Society of the Pacific Conference Series, CASA Architecture and Applications. p. 127

Mezger P. G., Altenhoff W., Schraml J., Burke B. F., Reifenstein III E. C., Wilson T. L., 1967, ApJ, 150, L157

Moscadelli L., Sánchez-Monge Á., Goddi C., Li J. J., Sanna A., Cesaroni R., Pestalozzi M., Molinari S., Reid M. J., 2016, A&A, 585, A71

Mottram J. C., Hoare M. G., Lumsden S. L., Oudmaijer R. D., Urquhart

J. S., Meade M. R., Moore T. J. T., Stead J. J., 2010, A&A, 510, A89

Mottram J. C., Hoare M. G., Lumsden S. L., Oudmaijer R. D., Urquhart J. S., Sheret T. L., Clarke A. J., Allsopp J., 2007, A&A, 476, 1019

Mottram J. C., Hoare M. G., Urquhart J. S., Lumsden S. L., Oudmaijer R. D., Robitaille T. P., Moore T. J. T., Davies B., Stead J., 2011, A&A, 525, A149

Price S. D., Egan M. P., Carey S. J., Mizuno D. R., Kuchar T. A., 2001, ApJ, 121, 2819

Reynolds S. P., 1986, ApJ, 304, 713

Rodríguez L. F., Garay G., Brooks K. J., Mardones D., 2005, ApJ, 626, 953

Rodriguez L. F., Garay G., Curiel S., Ramirez S., Torrelles J. M., Gomez Y., Velazquez A., 1994, ApJ, 430, L65

Sandell G., Goss W. M., Wright M., Corder S., 2009, ApJ, 699, L31

Sault R. J., Teuben P. J., Wright M. C. H., 1995, in Shaw R. A., Payne H. E., Hayes J. J. E., eds, Astronomical Data Analysis Software and Systems IV Vol. 77 of Astronomical Society of the Pacific Conference Series, A Retrospective View of MIRIAD. p. 433

Sault R. J., Wieringa M. H., 1994, AaPS, 108, 585

Seifried D., Pudritz R. E., Banerjee R., Duffin D., Klessen R. S., 2012, MNRAS, 422, 347

Shu F., Najita J., Ostriker E., Wilkin F., Ruden S., Lizano S., 1994, ApJ, 429, 781

Shu F. H., Adams F. C., Lizano S., 1987, Annual Review of Astronomy, 25, 23

Smith M. D., Rosen A., 2005, MNRAS, 357, 1370

Stahler S. W., 1988, ApJ, 332, 804

Stecklum B., Caratti o Garatti A., Linz H., 2012, in Carciofi A. C., Rivinius T., eds, Circumstellar Dynamics at High Resolution Vol. 464 of Astronomical Society of the Pacific Conference Series, Integral-Field Spectroscopy of the Young High-Mass Star IRAS 13481-6124. p. 369

Stecklum B., Kaufl H., , 1998, ESO Press Release

Thi W.-F., van Dishoeck E. F., Pontoppidan K. M., Dartois E., 2010, MNRAS, 406, 1409

Thompson R. I., 1984, ApJ, 283, 165

Tsinganos K., Ray T., Stute M., 2009, Protostellar Jets in Context

Urquhart J. S., Busfield A. L., Hoare M. G., Lumsden S. L., Clarke A. J., Moore T. J. T., Mottram J. C., Oudmaijer R. D., 2007, A&A, 461, 11

Urquhart J. S., Busfield A. L., Hoare M. G., Lumsden S. L., Oudmaijer R. D., Moore T. J. T., Gibb A. G., Purcell C. R., Burton M. G., Marechal L. J. L., 2007, A&A, 474, 891

Urquhart J. S., Figura C. C., Moore T. J. T., Hoare M. G., Lumsden S. L., Mottram J. C., Thompson M. A., Oudmaijer R. D., 2014, MNRAS, 437, 1791

Urquhart J. S., Hoare M. G., Lumsden S. L., Oudmaijer R. D., Moore T. J. T., Brook P. R., Mottram J. C., Davies B., Stead J. J., 2009, A&A, 507, 795

Urquhart J. S., Hoare M. G., Purcell C. R., Lumsden S. L., Oudmaijer R. D., Moore T. J. T., Busfield A. L., Mottram J. C., Davies B., 2009, A&A, 501, 539

Urquhart J. S., Moore T. J. T., Csengeri T., Wyrowski F., Schuller F., Hoare M. G., Lumsden S. L., Mottram J. C., Thompson M. A., Menten K. M., Walmsley C. M., Bronfman L., Pfalzner S., König C., Wienen M., 2014, MNRAS, 443, 1555

van der Tak F. F. S., Menten K. M., 2005, A&A, 437, 947

Voronkov M. A., Caswell J. L., Ellingsen S. P., Green J. A., Breen S. L., 2014, MNRAS, 439, 2584

Walsh A. J., Burton M. G., Hyland A. R., Robinson G., 1998, MNRAS, 301, 640

Wheelwright H. E., de Wit W. J., Oudmaijer R. D., Hoare M. G., Lumsden S. L., Fujiyoshi T., Close J. L., 2012, A&A, 540, A89

Wilson W. E., Ferris R. H., Axtens P., Brown A., Davis E., Hampson G., Leach M., Roberts P., 2011, MNRAS, 416, 832

Wolfire M. G., Konigl A., 1991, ApJ, 383, 205

Wood D. O. S., Churchwell E., 1989, ApJS, 69, 831

Wood D. O. S., Handa T., Fukui Y., Churchwell E., Sofue Y., Iwata T., 1988, ApJ, 326, 884

Zapata L. A., Palau A., Galván-Madrid R., Rodríguez L. F., Garay G.,

Moran J. M., Franco-Hernández R., 2015, MNRAS, 447, 1826

Zinnecker H., Yorke H., 2007, Annual Review of Astronomy, 45, 481